On the influence of batch-to-batch microstructural variations on tool wear when machining C38 micro-alloyed steel

Wear 562–563 (2025) 205632

Contents lists available at ScienceDirect

Wear

journal homepage: www.elsevier.com/locate/wear

On the influence of batch-to-batch microstructural variations on tool wear when machining C38 micro-alloyed steel

Charlie Salame, Amir Malakizadi *, Uta Klement

Department of Industrial and Materials Science, Chalmers University of Technology, SE-412 96, Gothenburg, Sweden

ARTICLE INFO

Keywords:
Tool wear
Micro-alloyed steel
Machinability
Inclusion

ABSTRACT

Sustainable machining in micro-alloyed carbon steels necessitates a thorough understanding of microstructural variations and their subsequent influence on the machinability of different batches. This research investigates the machinability variation between two batches of a modified pearlitic-ferritic C38 micro-alloyed steel with a similar nominal chemical composition, through correlation of their tool wear responses at different cutting conditions to discrepancies in the microstructure and non-metallic inclusions between both batches. One batch of steel exhibits enhanced machinability for all investigated cutting conditions, showing remarkably different levels of wear development under similar cutting conditions and spiral cutting lengths. The different wear responses are then compared in association with the thermo-mechanical loads and microstructural discrepancies, where the less machinable batch is determined to have a lower ferritic volume fraction, higher hardness, and more abrasive nitrides than the other batch.

1. Introduction

For a given set of cutting conditions and tool-workpiece combinations, a consistent and repeatable machining process requires a predictable tool wear progression to meet desired dimensional tolerances and surface integrity standards. However, slight changes in the material properties, arising from variations in the chemical composition (albeit within the standard specifications) and microstructural characteristics, may lead to unexpected tool wear behaviour and premature tool failure during machining process [1,2]. To mitigate such risk, cutting parameters and tool-change intervals are often selected conservatively at the expense of reduced productivity. Hence, it is of great interest to identify the specific material attributes that lead to the variations in tool wear behaviour when machining different batches of a given alloy. This knowledge facilitates a better utilisation of tools within the production line, enabling improved process planning that is tailored to a given batch of material with distinct chemical compositions and microstructural properties.

The batch-to-batch variation in steels can originate from the steel-making process itself, for example, due to slight variations in the material charge, type of melting process and the following refining steps, generally referred to as ladle metallurgy. The large-size oxide, sulphide and carbonitride precipitates are typically formed within the slag in the liquid phase, and/or in the last stage of solidification on the liquid/solid interfaces [3]. The distribution and type of carbides within the steel matrix are shown to substantially influence tool wear progression when machining steels [4,5]. While a small variation in amount, type and composition of non-metallic inclusions (NMIs) such as sulphides and oxides (within standard specifications) may not have a major impact on the mechanical properties of the workpiece material, they are shown to significantly influence the machinability of steels [6–9]. This effect is particularly evident in free-machining steels, where control over factors such as sulphide inclusion size and oxide content is exercised to enhance machinability [10,11]. Since the introduction of free-machining steels, research studies have focused on optimising steel machinability through deliberate manipulation of non-metallic inclusions in terms of composition, distributions, and shape factors. Advancements in ladle metallurgy techniques and the adoption of more sophisticated deoxidation methods have brought forth new grades of improved machinability – a practice commonly referred to as “inclusion-engineering” [12]. For example, by tailoring NMIs, it is possible to promote the formation of softer and more malleable inclusions, thereby mitigating the abrasive impact of certain inclusions on the cutting edge of the tool [13].

The material variation can also arise from the subsequent thermo-mechanical processes like rolling, forging and heat treatments due to their impacts on the microstructure development and thus the hardness

* Corresponding author.
E-mail address: amir.malakizadi@chalmers.se (A. Malakizadi).

https://doi.org/10.1016/j.wear.2024.205632
Received 27 June 2024; Received in revised form 27 October 2024; Accepted 5 November 2024
Available online 10 November 2024

and flow stress properties of a given alloy. Microstructural properties such as pearlite volume fraction and morphology (lamellar vs. spheroidised) are shown to influence the machinability of carbon steels. The consensus concerning pearlitic-ferritic steel is that the microstructure with smaller pearlite content and thus lower hardness level results in longer tool life when machining using carbide tools [14]. For example, Björkeborn et al. [15] compared the machinability of a case hardening steel with various microstructures and reported that tool life decreases as the pearlite content and its nodule size increases. Abouridouane et al. [16] observed that among two batches of a ferritic-pearlitic steel (C60), the material exhibiting a higher ferrite fraction and larger pearlitic lamellar spacing demonstrated improved machinability in terms of cutting force and chip formation characteristics. However, the effect of microstructural variations on tool wear behaviour during machining is most often investigated within the context of a specific batch of material subjected to different thermo-mechanical treatments. While this approach facilitates the examination of microstructural effects, it neglects the potential influence arising from alterations in chemical composition. This is particularly important for micro-alloyed steels containing small amounts of vanadium, titanium or niobium, where the nano-size carbonitride during rolling and subsequent thermal treatments largely control the grain size due to so-called pinning effect and thus the resulted microstructure [3,17]. These precipitates provide additional strengthening effects depending on their size and volume fraction, and therefore increase the hardness and tensile properties of the steel [18].

To best of our knowledge, the role of abovementioned aspects is not sufficiently investigated in previous studies. To this end, this study aims to enhance the understanding of batch-to-batch variations in a medium-carbon micro-alloyed steel and their influence on its machinability. Thus, a dedicated comparative analysis is performed on two batches of a C38 micro-alloyed steels, to discern the microstructural distinctions between them and the role they can play on tribological conditions on the tool surface. Face turning tests are performed on both batches using a coated cemented carbide tool under various cutting conditions and the resulting worn tool surfaces are compared. The differences in the tool wear response between both batches is then examined in light of the identified microstructural variances.

2. Experimental

2.1. Materials and characterisation procedures

The material under investigation is a vanadium micro-alloyed C38 steel. Two batches of this steel in the as-received condition – cylindrical bars with identical diameters (160 mm) and length (140 mm) – were used in this study in order to minimise any geometrical inconsistencies during the cutting tests. The steel bars, referred to as Batch A and Batch B herein, are provided from the same supplier at two different occasions, i.e., from two different melts. The chemical composition of each batch was identified using Wavelength Dispersive X-Ray Fluorescence Spectrometry as well as combustion and insert gas fusion techniques according to ASTM E 1019-18, ASTM E 752-21 standards. The chemical analyses indicated some differences in the amounts of micro-alloying elements: vanadium and titanium as well as nitrogen, albeit within the standard specifications. Batch A contains 24 %, 15 % and 13 % larger amount of titanium, vanadium and nitrogen, respectively.

To quantify the microstructural variations between the different batches, a dedicated characterisation of the workpiece materials was done to capture their micro-hardness, phase fractions and properties, and non-metallic inclusions. For this purpose, four metallographic samples were extracted from each batch, as shown in Fig. 1. The samples were extracted only from areas that would be subject to machining, so as to ensure the correlation of the material characterisation results to the tool wear characterisation. To detect any possible variations within each material's microstructure, two of the samples were extracted from a larger diameter of the bar, while the other two were extracted from a smaller diameter.

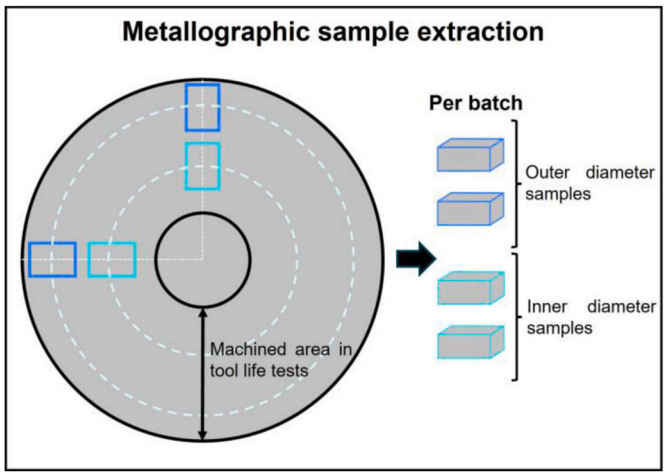

Fig. 1. Metallographic sample extraction for each batch of material.

Characterisation of the workpiece materials was done using scanning electron microscopy (SEM), energy-dispersive X-ray spectroscopy (EDS) as well as light optical microscopy (LOM). After polishing, each sample's microstructure was examined for non-metallic inclusions using the Zeiss Gemini 450 FEG-SEM equipped with the Oxford Ultim Max 100 silicon drift EDS detector. The chemical composition and distribution of inclusions was determined using the EDS feature analysis module (AztecSteel®) of the Oxford Aztec system, with a 15 kV acceleration voltage for the primary electron beam. The scheme for inclusion classification was selected to be the built-in "high quality steel" scheme, which classifies non-metallic inclusions based on certain thresholds of the obtained EDS compositions. This inclusion analysis was conducted on each of the 4 samples per batch. For each sample, the analysis was done on a total area of 5.5 mm^2 with the analysed frames randomly selected along the sample's entire surface, leading to a total analysed area of 22 mm^2 per batch. Since the analysis was performed over a statistically representative area, then the volume fraction of each inclusion class may be assumed equal to its area fraction [19].

Additionally, automated hardness testing (Vickers, 10 kgf test load) was performed on the polished samples using the Struers DuraScan-70 G5 hardness tester, with an average of forty-two indents per sample. The samples were then etched with Nital solution (2 % HNO_3 concentration) to expose the microstructural phases. Using light-optical microscopy (Leitz DRMX), a statistically representative area of at least 4 mm^2 per sample was captured at 50x magnification. The images were then processed to quantify the area fractions of the ferrite for each batch using image processing in MATLAB. Similar to the NMIs, the volume fraction of each microstructure may be assumed equal to its computed area fraction [19]. The average ferritic grain size was also obtained using the intercept method with a circular grid adopted from ASTM standard E112. The etched samples were also examined using SEM imaging with secondary electrons in order to visualize the pearlitic microstructure and measure the pearlite mean true interlamellar spacing according to the universal circular test grid method [20]. The lamellar spacing of at least 200 different pearlitic colonies were characterised for each batch using this methodology. After the machining tests, the rake and flank surfaces of the tool were examined using SEM with secondary electrons (SE) and backscattered electrons (BSE) imaging, as well as EDS analysis to reveal the underlying wear mechanisms.

2.2. Machining tests

In order to compare the tool wear behaviour when machining both batches, face turning operations were conducted using an EMCO TURN

365 CNC-lathe equipped with a three-component dynamometer (Kistler 9257A) for force measurements, as shown in Fig. 2a. No cutting fluid was supplied during the cutting tests in order to match the industrial application of the workpiece material. CVD-coated cemented tungsten carbide inserts (Seco Tools, DCMT 111T304-M3) and grade TP2501 were utilized for all cutting conditions. The selected tool grade consists of a mixed tungsten carbide and 6 % cobalt binder and is CVD-coated (Ti(C,N) + Al_2O_3). In addition, this tool grade includes a thin Cr-rich coating on the outer layer to enhance wear detection during the machining process. The tool holder used to mount these inserts was SDJCR2525M11, resulting in a 0° rake angle and 7° clearance angle.

The same experimental setup and cutting conditions, presented in Fig. 2b, were used for machining both batches of steel. The cutting speed was varied between 300 m/min, 400 m/min and 500 m/min while the feed rate and depth of cut were kept constant at 0.10 mm/rev and 1.0 mm for all cutting tests. At these cutting conditions, constant spiral cutting length (SCL) tests were performed, where each insert was used to machine a spiral cutting length of 1200 m. The cutting inserts were then inspected with the LEO 1550 Gemini SEM equipped with an Oxford X-Max silicon drift detector for EDS analysis. Three repetitions of each constant-SCL test were conducted to ensure the repeatability and validity of the results. The cutting conditions for the dedicated SCL-tests were selected based on the results of more extensive tool life tests conducted for both batches, as presented in the supplementary material. Further, the chosen cutting conditions were selected within the expected operational range for this tool-workpiece combination in industrial applications, offering a variation in cutting speed that influences the progression of tool wear and eventual tool life in both batches of steel.

3. Results

3.1. Microstructural characterisation of batches

The results of the workpiece characterisation of both batches are presented in this section and are discussed within the context of their effect on machinability. These include macro-properties such as hardness as well as microstructural features such as grain size, phase fractions and distribution and composition of inclusions.

Fig. 3 presents LOM micrographs showing the etched microstructure of both batches. As evident, both batches possess a pearlitic-ferritic microstructure, with an apparently finer grain structure at the external diameter, i.e. closer to the surface of the workpiece. It should also be noted that both batches revealed few colonies of bainite in similar quantities within their microstructures; however, they were only observed in inner diameter of the samples and their amount was deemed insignificant to have a considerable effect on the difference in machinability.

Batch B seems to possess a finer microstructure at both the inner and outer diameter of the sample as compared to Batch A. The mean intercept length is calculated as 7 μm and 6.3 μm for the inner and outer samples of batch A, respectively. In contrast, the mean intercept length in Batch B is 6.7 μm (4 % smaller) for the inner sample and 5.6 μm (12 % smaller) for the outer sample. These intercept values yield the average ferrite grain sizes summarised in Table 1 using the interpolation method described in the ASTM standard. The area percentage of ferrite in Batch B was calculated as 29 ± 2 % and 26 ± 3 % in inner and outer diameters, respectively, while for Batch A, the ferrite percentage was notably less at 18 ± 1 % and 19 ± 1 % at the respective regions. Additionally, pearlite-ferrite banding is observable in the outer diameter samples of both batches and becomes particularly visible in the inner diameter sample of batch B. Further characterisation of the microstructures was done in regard to the pearlite interlamellar spacing, where both batches yielded similar values for their average lamellar spacing. Batch A yielded an average mean true spacing of 0.21 μm and 0.19 μm at inner and outer diameters. The mean true interlamellar spacing of pearlite was 0.18 μm and 0.20 μm in the respective regions of the steel bar in Batch B.

With regard to the hardness measurements, the hardness of the inner and outer samples of Batch A were 239 ± 6 kg/mm^2 and 261 ± 7 kg/mm^2, respectively. For Batch B, the respective hardness measurements were 240 ± 12 kg/mm^2 and 241 ± 10 kg/mm^2. When comparing the two batches, it was determined that batches A and B have nearly similar hardness in the internal samples, with Batch A being just 1 % lower in hardness. Despite the apparently larger average grain size, the hardness of Batch A was slightly higher by 8 % than that of Batch B at the outer sample location. Table 1 summarises the results of microstructure analysis for both batches.

Fig. 4 shows some BSE micrographs of the most common groups of inclusions found in both batches, along with elemental maps and spectra analysis of the respective inclusions. In general, the examined inclusions within these two batches can be classified into nitrides, sulphides, oxides, and mixed inclusions. Mixed inclusions here are used to refer to complex inclusions that combine 2 or more of the main classes. These include oxysulphides, which consist of a combination between oxides, sulphides, and potentially nitrides. Samples of these mixed inclusions

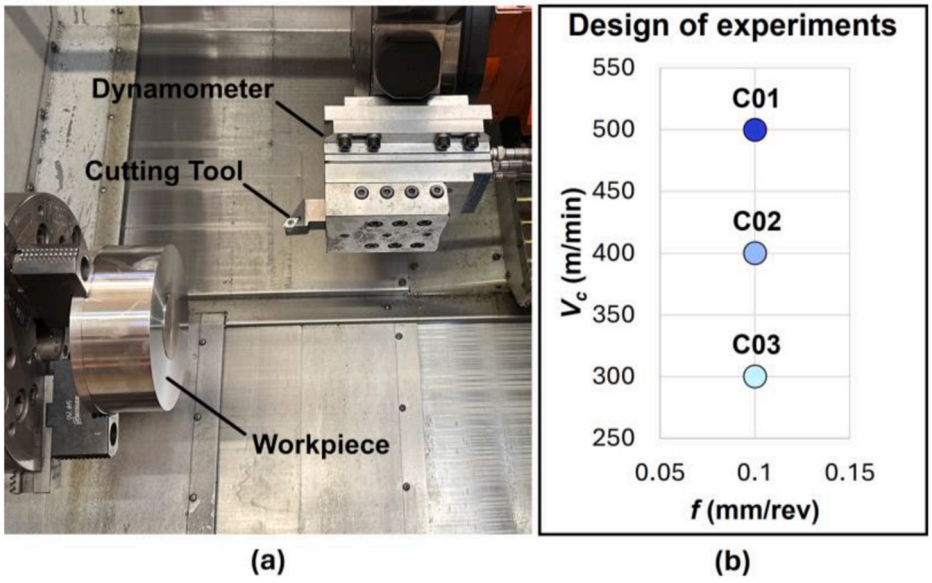

Fig. 2. Experimental setup showing the workpiece, cutting tool and dynamometer (a), design of experiments showing the different cutting conditions (b).

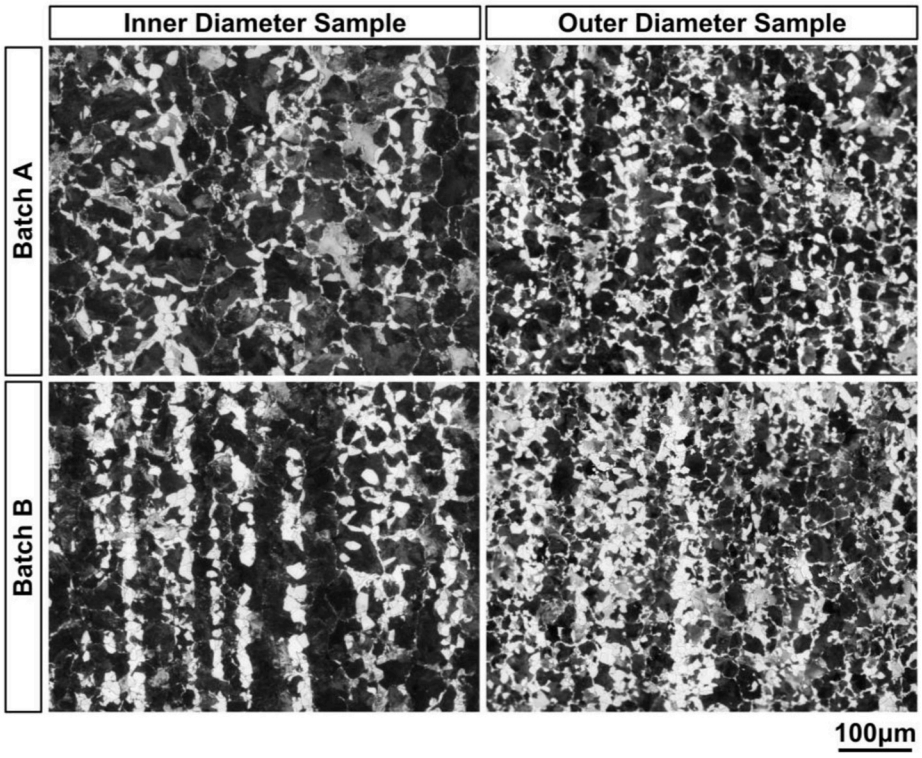

Fig. 3. LOM micrograph of etched surfaces of batches A and B at 50x magnification.

Table 1
Comparison of different microstructural characteristics and hardness in batches A and B.

Characteristics	Batch A		Batch B	
	Inner (8 mm^2)	Outer (8 mm^2)	Inner (8 mm^2)	Outer (8 mm^2)
Ferrite area percentage [%]	18 ± 1	19 ± 1	29 ± 2	26 ± 3
Pearlite lamellar spacing [µm]	0.21	0.19	0.18	0.2
Ferrite grain size [µm]	7.9	7.1	7.5	6.3
Hardness [kg/mm^2]	239 ± 6	261 ± 7	240 ± 12	241 ± 10

along with their elemental maps are shown in Fig. 4.

The results of inclusion analysis are presented in Fig. 5 and Table 2. The area fraction of each inclusion, which represents the fraction of the scanned area occupied by each class of inclusions, is plotted in Fig. 5. It should be noted that very few inclusions in the feature analysis were classified as pure oxides (<2 %), hence they were combined with the class of oxysulphides in the subsequent analysis. It is evident that sulphides – specifically manganese sulphides – occupy the largest fraction for both batches. For batch A, this is followed by Ti-Nitrides, manganese calcium sulphides then oxysulphides, respectively. For batch B, the next largest area fraction belongs to oxysulphides, followed by Ti-nitrides then manganese-calcium sulphides.

By comparing the area fractions between batches A and B, some major differences arise. While the MnS area fractions are fairly similar between both batches (only 8.5 % lower for Batch B) (as shown in Fig. 5), batch B actually possesses almost four times the number of these inclusions in A, as shown in Table 2. To yield the similar total area fraction, this difference in quantity is compensated for by the significantly larger average area per sulphide found in Batch A (6.2 μm^2) as compared to B (1.7 μm^2). Another striking difference for these types of inclusions is the difference in their aspect ratio, defined as the ratio between an inclusion's longer and shorter axis (i.e. an aspect ratio closer to 1.0 indicates a more circular inclusion). The aspect ratio of MnS inclusions in Batch A is on average 26 % higher, indicating more globular sulphide inclusions in Batch B. Thus, despite the similar total area fraction of manganese sulphides in both batches, Batch B possesses significantly more, smaller and more globular manganese sulphide inclusions than Batch A.

The difference in area fraction is more significant for (Mn,Ca)S inclusions, with these types of sulphides occupying 53 % less area of batch B than A (Fig. 5). In accordance, the quantity of these inclusions is 33 % higher in Batch A, with a 55 % larger mean area and 10 % lower aspect ratio compared to B. A similar difference in area fraction exists between the titanium nitride inclusions, where batch B trails A by 49 %. These nitrides exist in larger quantities in Batch A (37 % higher). Their mean area is also 47 % higher in Batch A, while their average aspect ratio does not differ between the batches. The larger number of nitrides in Batch A is consistent with the results of the chemical analysis.

Regarding oxysulphides, the inclusions detected in Batch B occupy more than double the area fraction compared to batch A (110 % higher) and are almost double in quantity (77 % higher). Their mean aspect ratio is identical and is the closest to 1.0 among all other types of inclusions, as expected for these kinds of inclusions which tend to be circular, as shown in Fig. 4. The potential effect of these oxysulphides on machinability of steel is quite complex and requires a more thorough analysis of their chemical composition. For this reason, the inclusions identified by AztecSteel® are superimposed on the pseudo-ternary phase diagram of system CaO-MgO-Al_2O_3-SiO_2 system containing 10 wt% MgO [21], as shown in Fig. 6. This figure also shows the stable phases and the liquidus isotherms. The detected oxysulphides using AztecSteel® contained up to 10 wt% SiO_2 and 10 wt% MgO and they were predominantly localised within the spinel region of the phase diagram for both batches.

3.2. Tool wear characterisation

To achieve a better understanding of the correlation between the microstructural batch variations, presented in section 3.1, and the

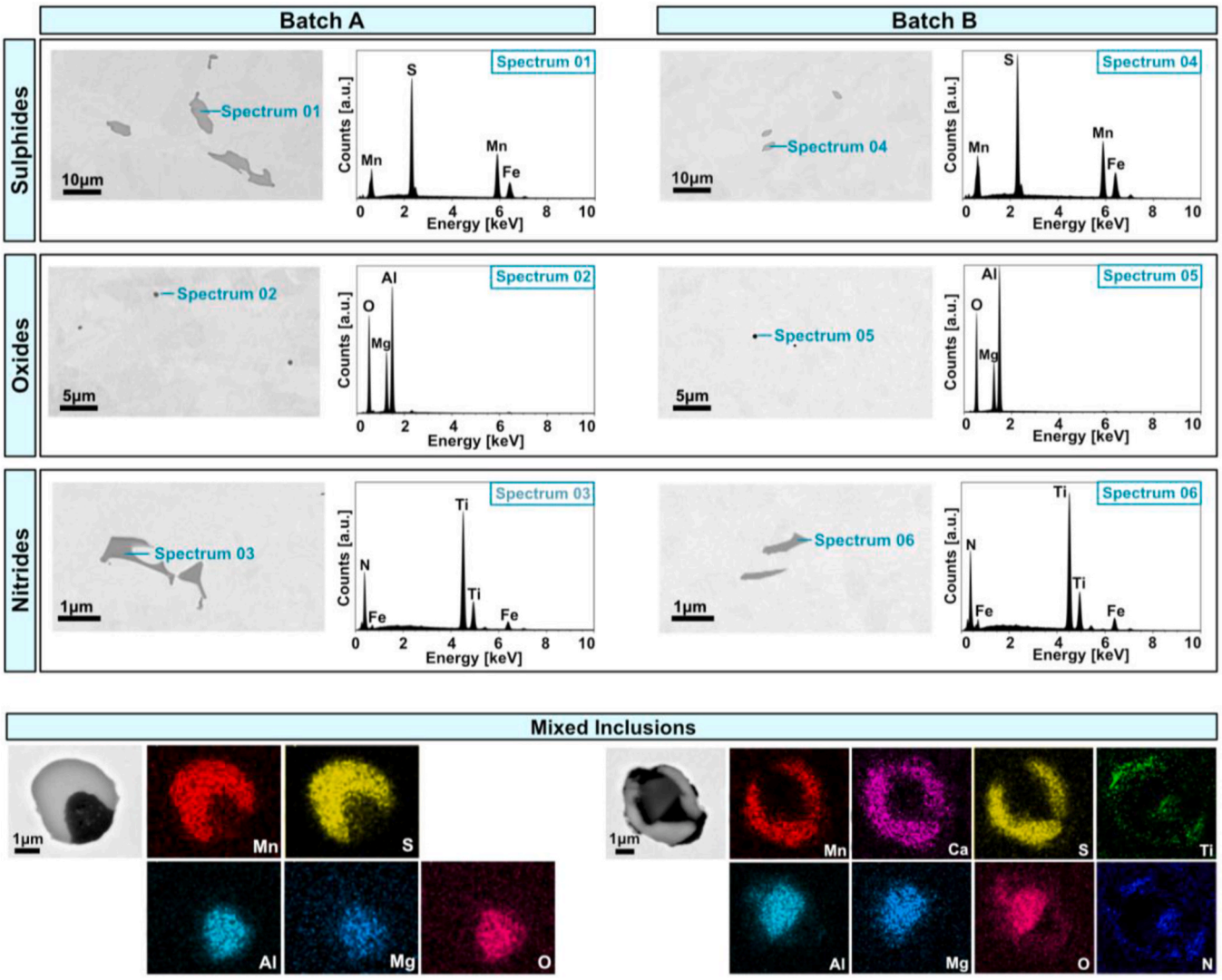

Fig. 4. Samples of the most common non-metallic inclusions found in batches A and B; nitrides, sulphides, oxides and mixed inclusions. BSE images and EDS spectra and maps acquired at 15 kV.

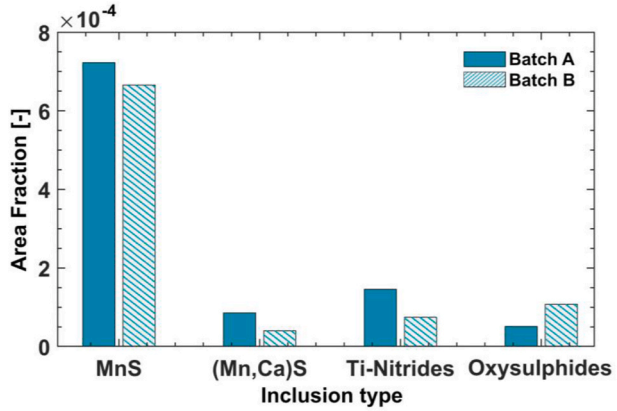

Fig. 5. A comparison of the area fraction (i.e., volume fraction) occupied by the different non-metallic inclusion classes between Batch A and B (scanned area is 22 mm^2 per batch).

difference in machinability, it is important to understand the active wear mechanisms that occur during the machining of each batch. For this purpose, the worn tools are examined in detail after machining both batches of steels under cutting conditions C01, C02 and C03, see Fig. 2.

Table 2
Comparison of different properties of each class of non-metallic inclusions in batches A and B.

Constituent	Property	Batch A	Batch B
MnS	Quantity [–]	2541	8236
	Mean area [μm^2]	6.2	1.7
	Mean aspect ratio [–]	2.9	2.3
(Mn,Ca)S	Quantity [–]	599	451
	Mean area [μm^2]	3.1	2.0
	Mean aspect ratio [–]	1.9	2.1
Ti-Nitrides	Quantity [–]	1431	1046
	Mean area [μm^2]	2.2	1.5
	Mean aspect ratio [–]	2.4	2.4
Oxysulphides	Quantity [–]	383	675
	Mean area [μm^2]	3.0	3.5
	Mean aspect ratio [–]	1.5	1.5

The BSE images of the different worn tools, designated by the cutting condition number and machined batch, are shown in Fig. 7. Table 3, presents the flank wear measurement results, including the mean values and variation ranges across three repetitions for the investigated cutting conditions.

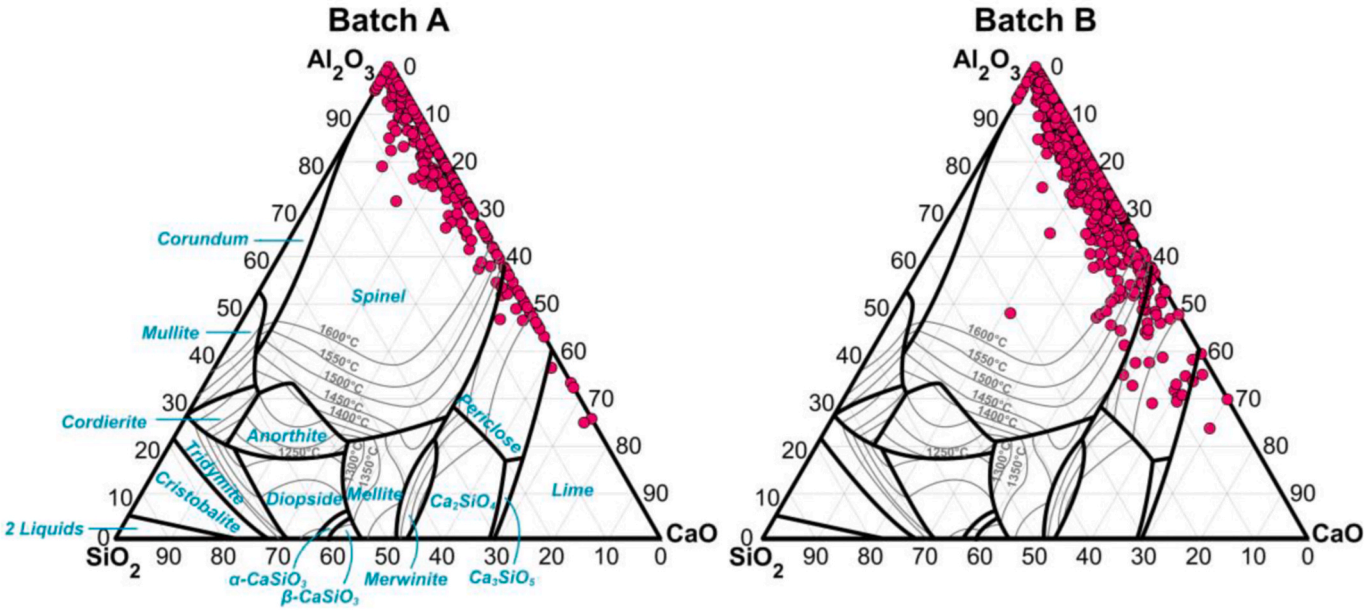

Fig. 6. The pseudo-ternary phase diagram of CaO-Al_2O_3-SiO_2 system containing 10 wt% MgO showing the compositions of the oxysulfide inclusions within the investigated steel batches.

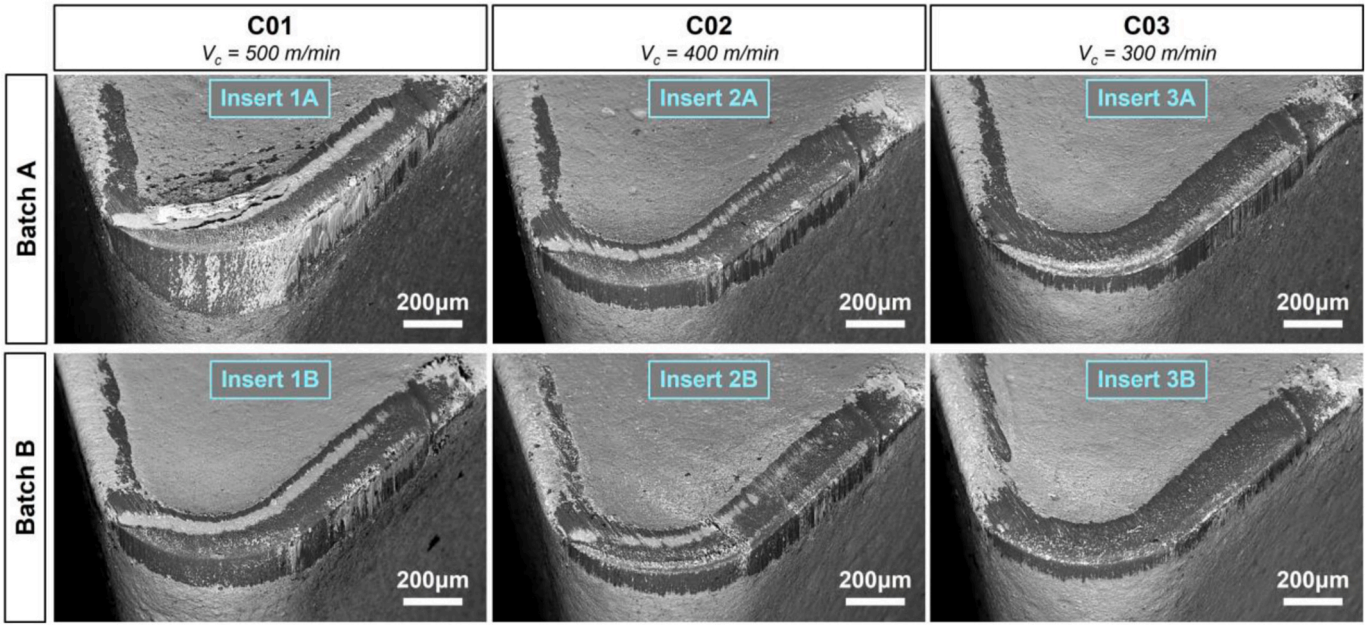

Fig. 7. SEM micrographs showing the worn tools after SCL of 1200 m machining both Batch A and B under the different cutting conditions (obtained using BSE at an acceleration voltage of 20 kV).

Table 3
Summary of flank wear measurements for the investigated cutting conditions.

Cutting conditions	Batch A	Batch B
	VB_{Bmax} (µm)	VB_{Bmax} (µm)
C01 (V_C = 500 m/min)	280 ± 35	194 ± 7
C02 (V_C = 400 m/min)	168 ± 5	153 ± 12
C03 (V_C = 300 m/min)	144 ± 6	101 ± 4

It is evident that the tool wear is significantly more advanced at the higher cutting speed (C01), followed by C02 then C03, despite the constant spiral cutting length between all inserts. This is justified by the increase in thermal loads on the tool surfaces due to the higher cutting speed. It is also evident that after the same duration of cut, the tool wear is notably more advanced for the tools used to machine Batch A than those used for Batch B. This is especially clear for cutting conditions C01 and C03, where differences in flank wear and crater wear are particularly evident.

The relative resistance of various workpiece materials to deformation during cutting, as indicated by cutting forces, provides insights into the thermo-mechanical loads experienced by tool surfaces. Notably, the average cutting forces in the initial 10 s of cut, presented in Fig. 8, show a very slight variation between the cutting forces in batches A and B for all three cutting conditions. While the average cutting and feed forces were slightly higher when machining Batch B at cutting condition C01, no major difference was noted between the measured forces for Batch A

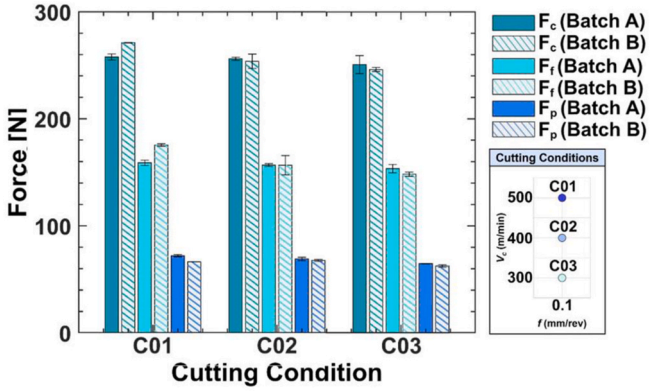

Fig. 8. Average cutting, feed and passive forces during the first 10 s of machining time.

and Batch B under cutting conditions C02 and C03.

At the lowest cutting speed, inserts 3A and 3B exhibit similar tool wear mechanisms to differing extents. A more dedicated analysis of both the rake and flank surfaces of these tools is presented in Fig. 9, including EDS maps that show the chemical composition of these surfaces after machining. The presented elemental EDS maps pertain to the main coatings and substrate material on the tool as well as any adhered or transferred layer from the workpiece. All EDS maps presented in this research were confirmed with point EDS analysis at the relevant locations (available in the supplementary material). By comparing the rake surfaces of both inserts, it is seen that the alumina coating layer is intact in both inserts, appearing in a dark grey colour in the BSE micrographs, and only the outmost thin Cr-rich coating layer is removed. Towards the end of the depth of cut on the main cutting edge, both inserts show an adhesion of workpiece material. Beyond that, only insert 3A shows a further exposed area of its alumina coating. Smearing of the workpiece material can be observed on the rake surface of both inserts, notably more in the case of insert 3B, as indicated by the areas of lightest grey colour in the BSE micrographs. Further, both inserts show a concentration of manganese and sulphur at the cutting edge, as seen in the EDS elemental maps. In the case of insert 3B, the manganese sulphide inclusions seem to also be spread across a larger fraction of the crater area, as opposed to being more localised on the cutting edge in insert 3A. With regard to the wear on the tools' flank surfaces, insert 3A clearly exhibits a higher depth of maximum flank wear. This observation is valid for all repetitions of this cutting condition, where VB_{Bmax} is measured at 144 ± 6 μm for the inserts used to machine batch A, while VB_{Bmax} for batch B is 29 % lower at 101 ± 4 μm. Similar to the rake face, the flank of insert 3B shows a higher amount of adhered workpiece material than insert 3A, as depicted by the EDS maps. Manganese sulphide appears on the flank face near the cutting edge and around the lower boundaries in both inserts.

Closeup SEM images of the flank side of both inserts are presented in Fig. 10. The identification of what appears to be grooves is apparent on the flank side of both inserts on the alumina coating layer. The examination of the worn surfaces at higher magnifications also indicates the presence of micro-cracks and micro-grooves in the alumina coating layer, as observed in Fig. 10. These cracks were formed when machining both batches of material and appeared on both rake and flank faces exposed to the chip or workpiece material.

For the cutting speed of 400 m/min (C02), the tool wear patterns on the rake and flank surfaces of the tools were similar to those observed at

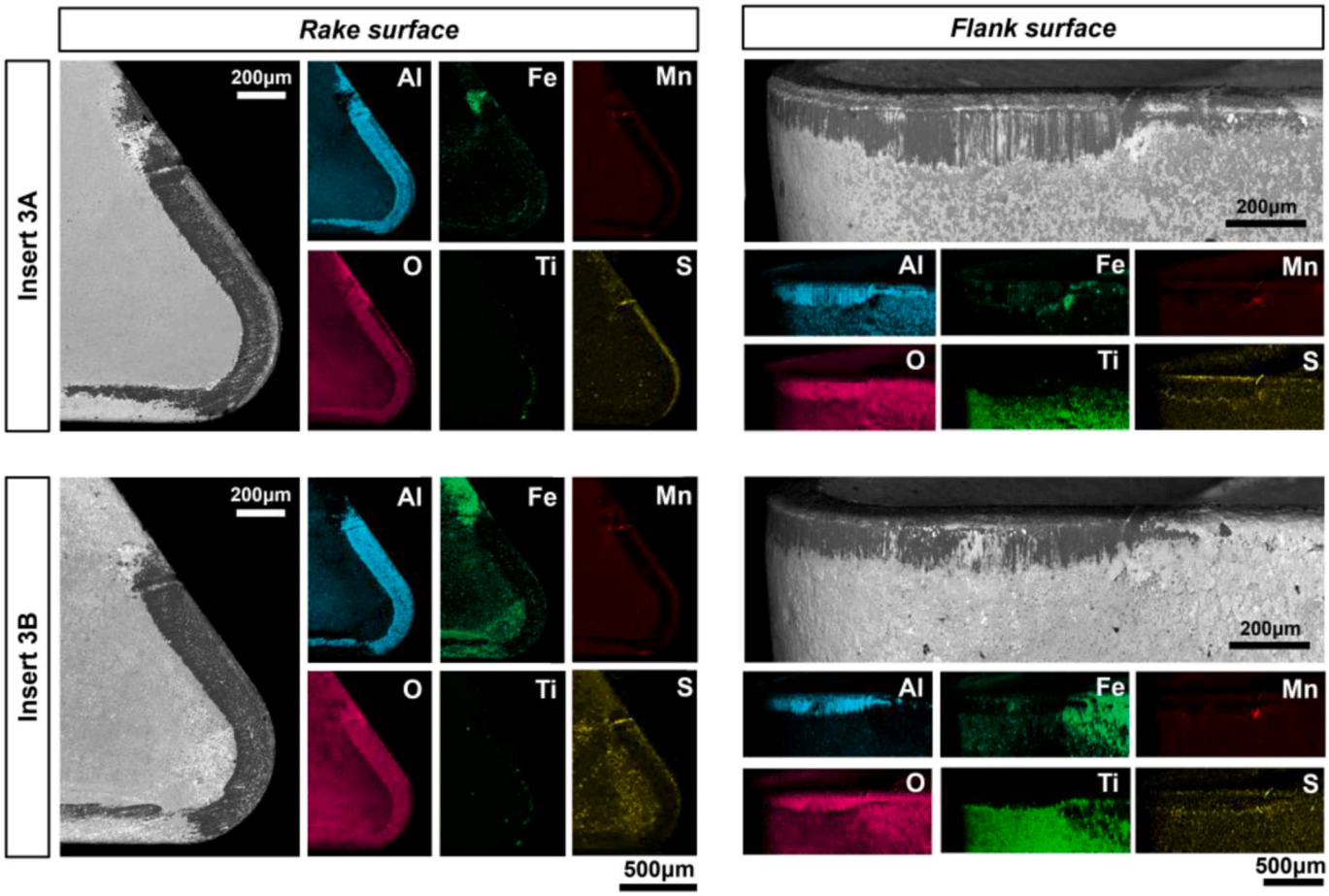

Fig. 9. SEM BSE imaging and EDS map analysis of the tools' rake and flank surfaces for cutting condition C03.

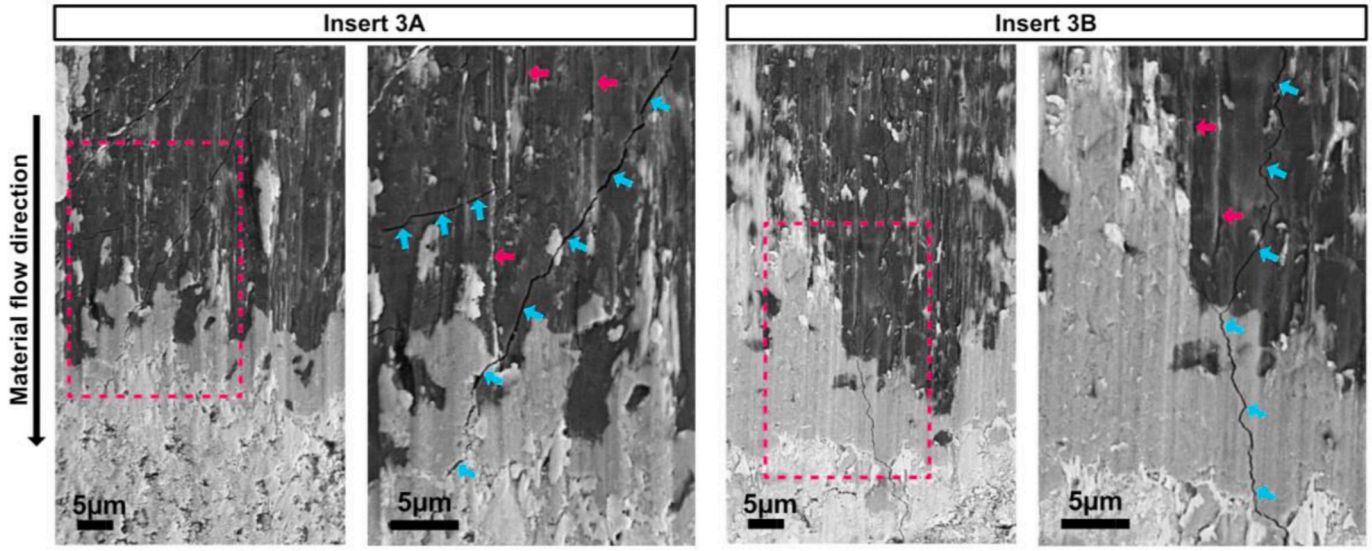

Fig. 10. SEM SE image of the flank face of insert (SE image obtained at 10 kV).

the lower cutting speed (C03). Fig. 7 depicts an overview of both inserts 2A and 2B after machining. At this cutting condition, a spiral cutting length of 1200 m causes both inserts to expose the underneath Ti(C,N) coating layer on the rake face, observed as a lighter grey strip within the darker grey alumina coating. However, on the flank side, the Ti(C,N) coating is only apparent for insert 2A, as seen in the SEM images and EDS maps in Fig. 11. Further, the maximum flank wear depth for the inserts used to machine batch A is 168 ± 5 µm, while for batch B, it is 153 ± 12 µm (9 % lower) at the same spiral cutting length. Concentrations of manganese and sulphur were also detected on the cutting edge for both inserts, as well as at the asperities of the exposed alumina coating on the flank side. At this cutting condition, a qualitative assessment of the EDS maps shows a more prominent concentration of sulphur in insert 2B.

The distinction in machinability between both batches becomes very clear for the highest cutting speed, as depicted in Fig. 12. On the rake side, crater wear is significantly more advanced in Batch A, where insert 1A shows an established crater that has exposed the different coatings as well as the underlying substrate material. The EDS maps confirm the exposure of the alumina and Ti(C,N) coating, as well as the tungsten carbide substrate in the crater (along with its cobalt binder). Batch A also leads to additional spalling of the coating, which exposes the alumina and Ti(C,N) coatings in the vicinity of the main crater. The spalling observed in insert 1A indicates the occurrence of plastic deformation wear at the investigated cutting condition.

On the flank side of the tools, the maximum flank wear depth measures 280 ± 35 µm and 31 % lower at 194 ± 7 µm for batches A and B, respectively. Notably, the location of the maximum flank wear is near the nose of insert 1A in contrast to insert 1B, where it develops more-or-less equally along the depth of cut for insert 1B. At this cutting condition, the Ti(C,N) coating is exposed in both inserts and the development of a manganese layer is evident within the flank wear area.

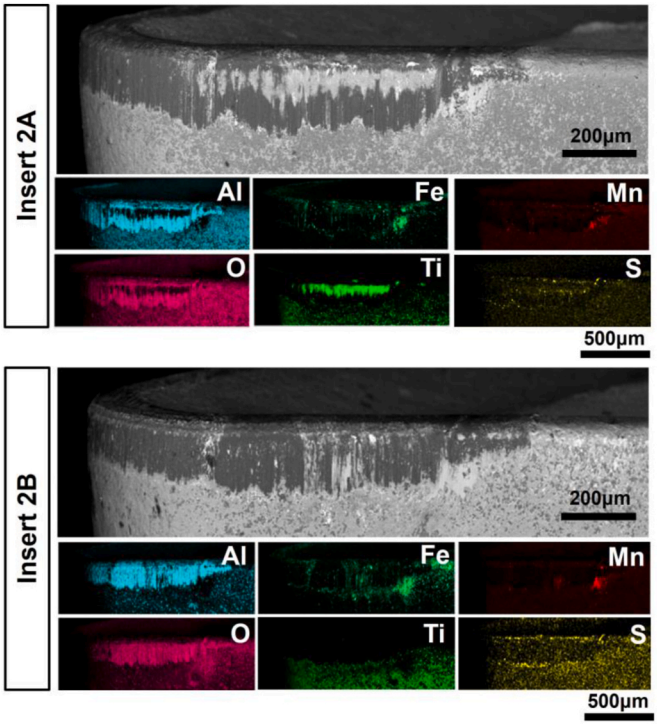

Fig. 11. SEM BSE imaging and EDS map analysis of the inserts' flank surfaces for cutting condition C02.

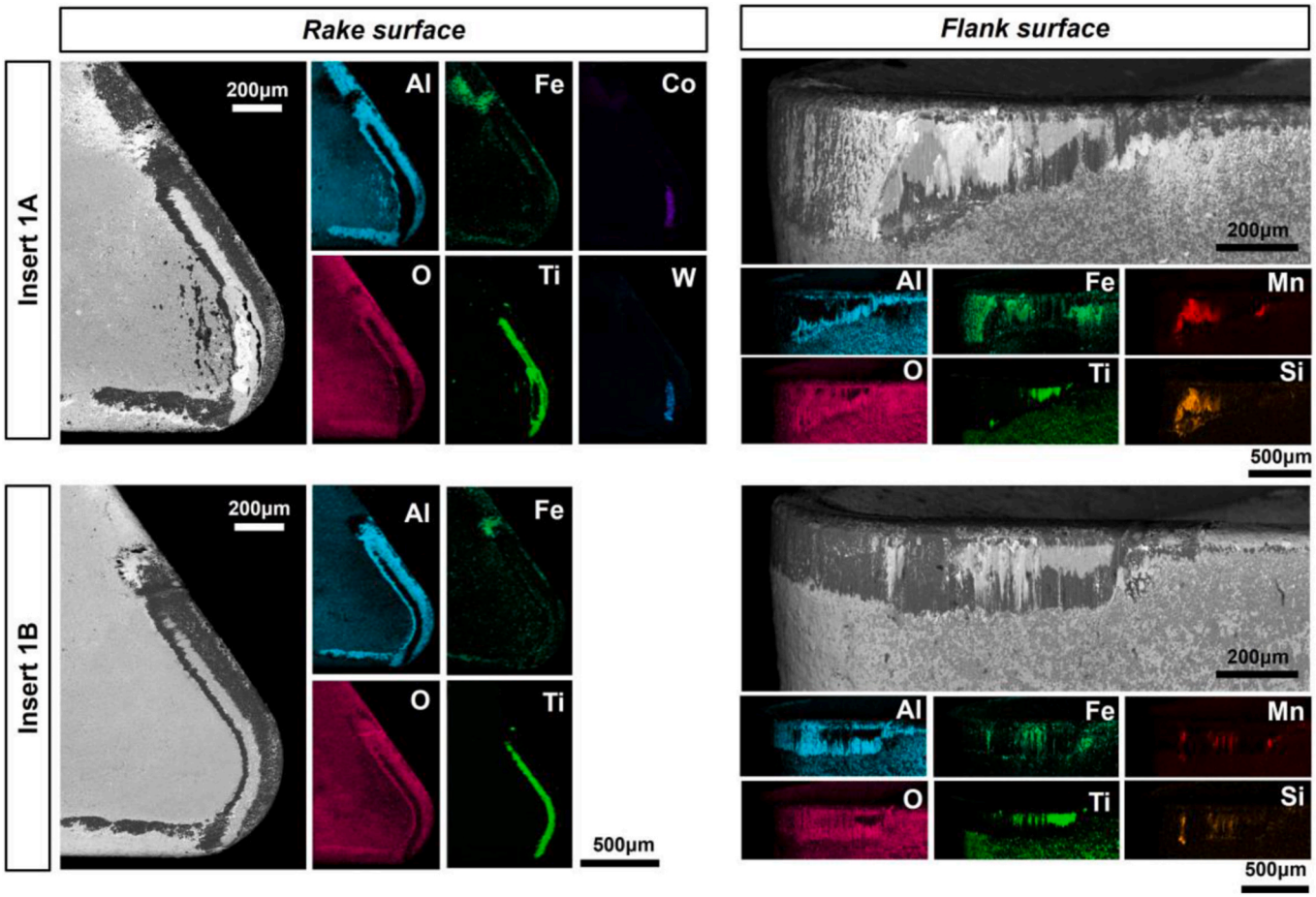

Fig. 12. SEM BSE imaging and EDS map analysis of the rake and flank surfaces for cutting condition C01.

4. Discussion

4.1. Influence of the microstructural characteristics

In order to shed light on the influence of microstructural variations on tool wear mechanisms, their impact on the thermo-mechanical loads on the tool surface is to be determined. Fig. 13 shows the role of distinct microstructural characteristics on the room temperature flow stress at a constant strain of 0.2, i.e. at 20 % deformation, calculated based on the Iso-work increment assumption accounting for different strain evolution in soft ferrite and the markedly harder pearlite such that the mechanical work increment in each constituent remains equal [22]. The implemented model accounts for the effect of ferrite grain size (d_α) and its volume fraction (v_α), the pearlite lamellar spacing (λ) and the size (r) and volume fraction (v_p) of the nano-size precipitates in micro-alloyed steels to estimate the flow stress response of the heterogeneous ferritic-pearlitic microstructure [23,24], the details of which are presented in Appendix.

As evident, the variations in the size and amount of the carbonitride precipitates have a large impact on the flow stress (tensile properties) of

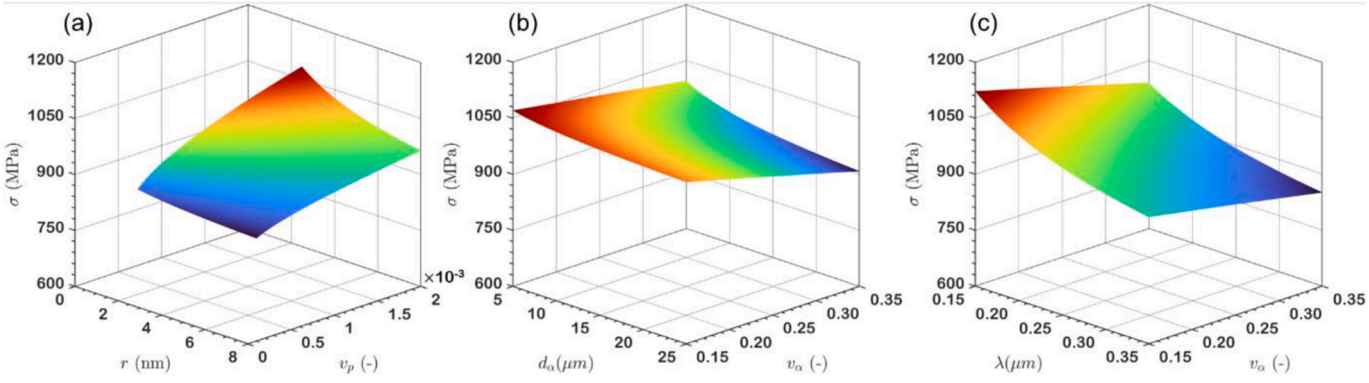

Fig. 13. The influence of precipitate size and volume fraction on flow stress at 20 % deformation for a pearlitic-ferritic microstructure with $\lambda = 0.2$ µm, $d_\alpha = 15$ µm, and $v_\alpha = 0.3$ (a), the influence of ferrite grain size and amount on flow stress at 20 % deformation for a pearlitic-ferritic microstructure with $\lambda = 0.2$ µm, $r = 5$ nm, and $v_p = 0.001$ (b), the influence of ferrite grain size and pearlite interlamellar spacing on flow stress at 20 % deformation for a pearlitic-ferritic microstructure with $d_\alpha = 15$ µm, $r = 5$ nm, and $v_p = 0.001$ (c).

the micro-alloyed steels. While decreasing grain size and volume fraction of ferrite, both result in an increase in the flow stress properties of ferritic-pearlitic steels. The major impact on flow stress holds for interlamellar spacing of pearlite. As shown in Fig. 13c, the flow stress at 20 % deformation increases from ~940 MPa to ~1120 MPa with decreasing pearlite interlamellar spacing from 0.35 μm to 0.15 μm, respectively, given all other microstructural parameters are constant: $v_\alpha = 0.15$, $d_\alpha = 15$ μm, $r = 5$ nm, and $v_p = 0.001$.

Paired with the results of microstructure analysis detailed in Table 1, this model offers an explanation for the increased hardness found in the outer sample of Batch A given the smaller volume fraction of ferrite, and potentially larger volume fraction of precipitates as compared to those of Batch B (due to a smaller amount of Ti and V in Batch B). This model can also explain the small hardness variations observed across the diameter in Batch B with only a marginal difference in ferrite content and ferrite grain size. Moreover, given that the size and volume fraction of ferrite showed minimal variation across the sample diameter in Batch A, the rather significant rise in hardness within the outer samples in this steel batch implies that it is predominantly influenced by the dimensions and volume fraction of carbonitride precipitates. This is consistent with the microstructural findings presented in Fig. 3, which reveal smaller pearlite nodule sizes in the outer diameter of Batch A. The overall finer microstructure in outer samples in this figure would suggest a higher volume fraction of precipitates near the surface of the workpiece, effectively pinning the recrystallized austenite grains during and after the rolling process.

Given the uncertainty surrounding the volume fraction and dimensions of carbonitride precipitates, providing an exact estimation of the flow stress properties for Batch A and Batch B is not possible. However, following the model-based evaluation of flow stress presented above, which relies on the documented microstructural characteristics detailed in Tables 1 and it is reasonable to infer that machining of Batch A would result in higher heat generation at a given cutting speed due to a higher strain hardening behaviour in this batch of material with an expectedly larger volume fraction of nano-size precipitates. Moreover, the physics-based flow stress model reveals a higher strain hardening behaviour in a material with a larger volume fraction of pearlite (see Fig. 13b). Under the assumption that the microstructural variations within the range shown in Table 1 do not greatly influence the thermal conductivity of investigated batches of steel, it can be expected that machining Batch A would result in higher cutting temperature. In fact, a higher amount of ferrite in Batch B would result in a somewhat higher thermal conductivity in this material, as the thermal conductivity of ferrite is larger than that of pearlite [25,26]. These would partly explain the lower wear evolutions observed when machining Batch B (see Figs. 7 and 12), despite a marginal difference in the cutting forces between the batches. This observation is in line with the previous reports on machinability of ferritic-pearlitic steels, indicating higher wear rates of carbide tools when machining steels with a larger amount of pearlite and higher hardness levels [14,15]. It is worth noting here that, in addition to the flow stress of the workpiece material, which determine its resistance to shear deformation, the cutting force is typically affected by several other factors, including the material ductility (i.e. strain to fracture) and the tribological conditions at the tool-chip interface – both of which are affected by the material's microstructural characteristics. As a result, scenarios may arise in which machining of a steel batch with the higher strength and lower ductility produces the cutting forces comparable to that of another batch with the lower strength, but higher ductility – as reported in the previous investigations [1,2]. This could explain a marginal difference observed in the measured cutting forces between the batches, despite an expectedly higher strain hardening response when machining Batch A.

4.2. Influence of the inclusion properties

The influence of non-metallic inclusions on machinability stems from their different modes of actions. The deformable and malleable NMIs like MnS and (Mn,Ca)S can function as stress raisers in the primary shear plane, creating voids at the interfaces between the inclusion and the matrix. As deformation progresses, these inclusions elongate along the shear direction, facilitating the propagation of cracks and aiding in chip breaking [12,27–29]. This can, in turn, reduce the contact area between the cutting tool and the formed chip, thereby decelerating tool wear progression [30]. Globular MnS inclusions are known to be more beneficial for chip formation than elongated sulphides since voids formed at the inclusion-matrix interface in a globular inclusion do not tend to reweld during deformation [31]. In regard to the formation of a lubrication layer, Ca-treated sulphides tend to exhibit better stability than the untreated inclusions, owing to their higher hardness; however, the higher hardness itself may have an undesirable effect on machinability [32]. Batch B, despite having a slightly lower total area fraction of manganese sulphides, possesses significantly more, smaller and more globular manganese sulphide inclusions than Batch A as shown in Table 2. While these three distinct characteristics, i.e., larger quantity, smaller size, and more globular shape, have all been demonstrated to enhance the machinability of steels [33], no major differences were observed in chip breakability or in the contact areas between the tool and chip when machining Batch A and Batch B (see Fig. 7). Hence, the positive impact of sulphide inclusions on the machinability of Batch B remains uncertain despite some differences in the deposited MnS layer on tool surfaces. Moreover, the manganese sulphides detected at lower cutting speeds (see Figs. 9 and 11) seem to exhibit less stability at higher cutting speeds due to their increased formability at elevated temperatures, in line with previous reports [34]. Instead, at this cutting condition, the formation of (Mn,Si)-rich layers occurs on the flank side of both cutting tools. This result matches previous findings by Opitz et al. [35], who reported the formation of Si-rich layers on carbide cutting tools.

In contrast to malleable sulphide inclusions, the non-deformable hard inclusions such as spinel oxides and nitrides would fracture rather than deform [12]. These hard inclusions come in contact with the tool's surfaces and can induce micro-rupturing of the tool coatings, resulting in their detachment from the tool and a subsequent loss of tool coating [36]. Hard oxide inclusions such as Al_2O_3, SiO_2 and $3Al_2O_3 \cdot SiO_2$ tend to fracture during machining and remain as hard fragments within the steel matrix, which can promote abrasive wear on the tool and thus be detrimental to the machinability [30,37]. On the other hand, oxy-sulphides are shown to have a positive influence on the machinability of steels compared to pure oxides, owing to their reduced abrasiveness due to the sulphide shell [27,38]. The calcium treatment of carbon steels, which promotes a transformation of harder oxides into softer calcium-rich oxides such as anorthite $CaO \cdot Al_2O_3 \cdot 2SiO_2$ and gehlenite $2CaO \cdot Al_2O_3 \cdot SiO_2$, are also shown to improve the machinability of steels [2,27]. These inclusions possess lower melting points and better visco-plastic properties, enabling them of forming more stable protective lubrication layers on the cutting tool [12,30,39,40].

The grooves appeared on the flank wear lands, shown in Fig. 10, give an indication of abrasion on the tool surfaces when machining both batches of steel. The substantial larger amount of abrasive TiN inclusions in Batch A – with comparable high-temperature hardness as that of alumina [41] – can effectively account for the higher wear progression observed when machining this batch of steel. In effect, these nitrides can play a major role in the delamination of alumina and Ti(C, N) coating layers on the rake face. With the gradual removal of alumina and Ti(C,N) coating layers during the machining process, a larger amount of heat is transferred into the tool substrate, increasing the likelihood of plastic deformation of the cutting edge, as observed in insert 1A (see Figs. 7 and 10). Hence, despite the formation of this (Mn,

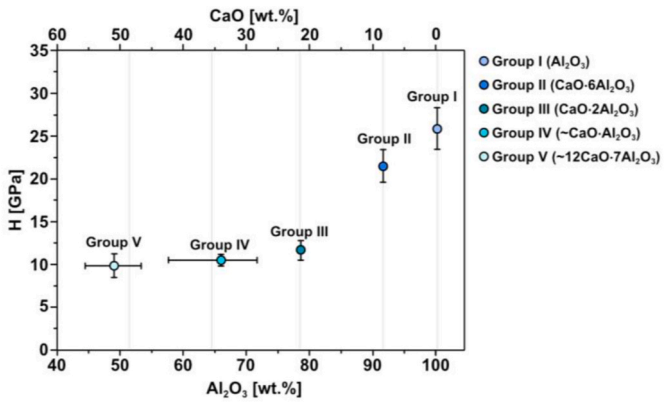

Fig. 14. Average hardness of common non-metallic inclusion groups in the $CaO\text{-}Al_2O_3$ system, obtained using the nanoindentation method – this figure is regenerated using the data presented in [42].

Si)-rich protective layer on both inserts 1A and 1B, the insert used for machining batch A showed considerably larger maximum flank wear width.

In contrast, neither flaking nor significant crater wear were noticeable on the rake face of insert 1B. While Batch B does contain a higher quantity of oxysulphides, the difference in their composition seems to act in favour of Batch B, possibly due to the higher quantity of Ca-rich oxides observed in the ternary diagrams (see Fig. 6). A recent investigation employing nanoindentation to assess hardness of Al_2O_3-CaO inclusions in iron revealed that the hardness of pure Al_2O_3 inclusions decreases from 26 ± 2.5 to 8 ± 2.0 GPa with an increase in concentration of CaO [42], as shown in Fig. 14. This implies that those pure oxides and oxysulphides in Batch B with concentrations of CaO larger than 20 wt% would play a minor role in wear by abrasion. This is in agreement with previous research that determined the positive influence of Ca-rich oxides on machinability [43]. The ability of these Ca-Al oxides to be deformed into fine elongated inclusions and form protective layers during machining has also been reported in previous research [12]. However, recent studies showed that the alumina coating can react to form calcium aluminate, spinel $MgAl_2O_4$ and calcium magnesium aluminate in presence of calcium- and magnesium-rich oxides and oxysulphides [44]. Once such chemical reactions occur at the high interface temperatures, the hardness of the alumina coating is substantially reduced, promoting the formation of grooves, and faster removal of the coating. This is in line with the isotherms shown in the pseudo-ternary diagram (Fig. 6), indicating lower liquidus temperature for the mixed Al_2O_3-SiO_2-CaO oxides as compared to that of pure alumina.

Fig. 15 illustrates the main findings of this investigation, summarising the relative impact of various microstructural characteristics that would contribute to the improved machinability of Batch B in this study. It is worth to note that, despite previous attempts to isolate the effects of individual microstructural characteristics – such as pearlite lamellar spacing, pearlite content, or ferrite grain size – on the machinability of pearlitic-ferritic steels [14–16], it is essentially impractical to reproduce a specific microstructure with a single defined characteristic without simultaneously altering other related properties [45–47]. This limitation becomes particularly critical in micro-alloyed steels, where variations in the thermal history simultaneously impact multiple parameters, including austenite grain size (due to the so-called pinning effect of nano-size precipitates [48]), pearlite and ferrite content, and the volume fraction and size of carbonitrides. These factors exert a collective impact on the flow stress properties of pearlitic-ferritic steels, as illustrated in Fig. 13, which urges the development of advanced microstructure-sensitive models for the machinability assessments.

The physics-based model adopted here to estimate flow stress of the medium carbon micro-alloyed steels does not account for thermal softening, dynamic strain ageing and strain rate hardening effects. The batch-to-batch microstructural variations can have a significant influence on the properties of these grades of steel at high temperatures and strain rates, the effects of which are not included in this model. To achieve a comprehensive understanding of the role of microstructural characteristics on the machinability of medium carbon micro-alloyed steels, it is essential to incorporate the aforementioned factors into the physics-based flow stress models. Moreover, given the significant impact of nano-size carbonitride precipitates on the flow stress properties of micro-alloyed steels, their dimensions and volume fractions should be determined either using the advanced material characterisation techniques or by thermodynamic/kinetic simulations [49,50]. The latter requires a thorough knowledge of thermo-mechanical processes involved along the value-chain such as rolling/forging temperature, subsequent cooling conditions and deformation ratio. In addition, the worn surfaces should be examined using high resolution techniques to

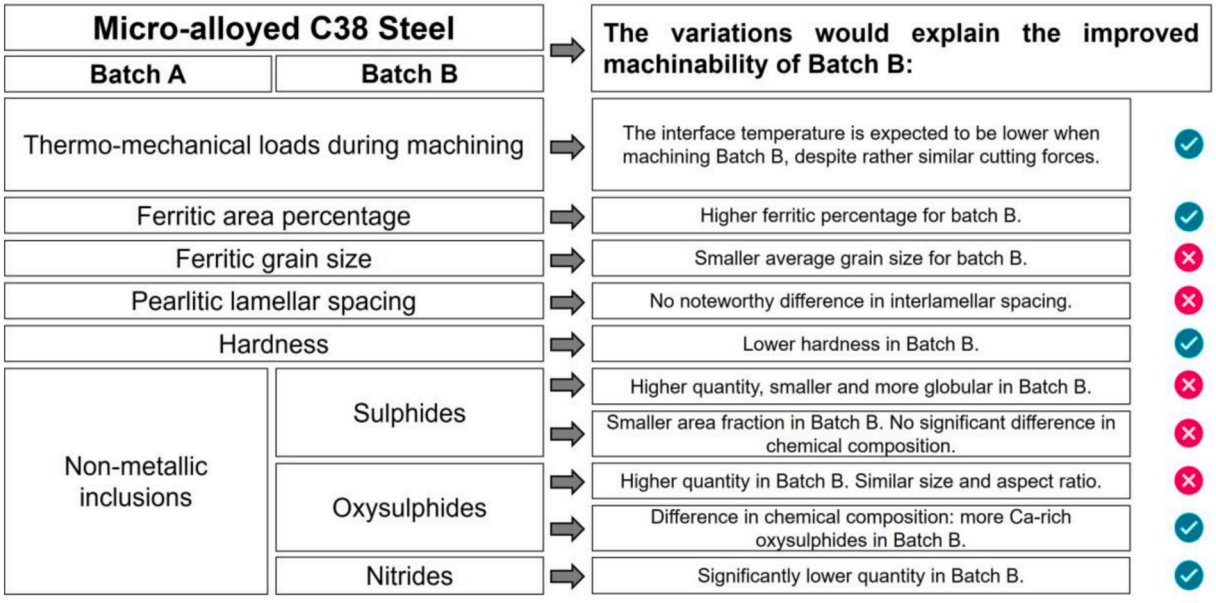

Fig. 15. Summary of the link between investigated features and the machinability (tool wear behaviour).

shed light on the impact of inclusion chemistry on degradation of Al_2O_3–Ti(C,N) coatings.

5. Conclusions

This research investigates the effect of microstructural variations in different batches of medium-carbon micro-alloyed steel on the tool wear during machining. A dedicated microstructural analysis of the workpiece materials is employed to quantify the differences between the two batches, after which constant spiral cutting length tests are performed to compare the tool life and wear mechanisms active during the machining of both batches. Supported with the model-based estimation of flow stress of precipitate strengthened pearlitic-ferritic microstructure, the following conclusions can be drawn.

- The machinability of nominally identical steels can vary significantly between different batches; the machining of Batch A and Batch B under identical cutting conditions led to notably less tool wear for Batch B for all investigated cutting conditions. Significant differences in flank and crater wear progression are observed for all cutting conditions.
- The microstructure characteristics of the workpiece material indicated notable differences in volume fractions of ferrite, micron-size titanium nitrides and oxysulphides between Batch A and Batch B.
- The model-based estimations indicated that the flow stress of the micro-alloyed steels is largely affected by the size and volume fraction of nano-size carbonitrides, pearlite volume fraction as well as the pearlite interlamellar spacing. The ferrite grain size also has an impact, however less profound.
- Despite the rather similar cutting forces, the cutting temperature is expected to be lower when machining Batch B due to a lower volume fraction of pearlite, a potentially lower amount of nano-size carbonitrides, and in overall, a lower hardness in this batch of steel.
- Under the range of cutting conditions investigated in this study, the disparities in the volume fraction, quantity, size and aspect ratio of MnS and (Mn,Ca)S sulphides between the steel batches did not demonstrate a major impact on enhanced machinability of Batch B as compared to that of Batch A.
- The notable increase in wear progression observed in Batch A was largely attributed to its significantly larger volume fraction and size of hard titanium nitrides, in effect resulting in higher wear by abrasion during machining in this material. The larger volume fraction of oxysulphides in Batch B did not result in higher wear progression in this batch of steel. Despite larger amount, the hardness of most oxysulphides in Batch B is not sufficiently high to have a major impact on wear by abrasion.
- The likelihood of chemical reaction between the tool and oxysulphide inclusions in Batch A and Batch B, and the effect that may have on the degradation of tool coatings needs to be investigated in more depth in the future studies.

CRediT authorship contribution statement

Charlie Salame: Writing – original draft, Visualization, Validation, Methodology, Investigation, Formal analysis, Data curation, Conceptualization. **Amir Malakizadi:** Writing – review & editing, Visualization, Validation, Supervision, Software, Resources, Project administration, Methodology, Funding acquisition, Formal analysis, Data curation. **Uta Klement:** Writing – review & editing, Validation, Supervision, Investigation.

Declaration of competing interest

The authors declare the following financial interests/personal relationships which may be considered as potential competing interests: Amir Malakizadi reports financial support was provided by Sweden's Innovation Agency. If there are other authors, they declare that they have no known competing financial interests or personal relationships that could have appeared to influence the work reported in this paper.

Acknowledgements

This study was part of the WEAR-FRAME project funded by Vinnova (Sweden's Innovation Agency) under FFI program (Project No.2020-05179). The supports received from the Chalmers Area of Advance – Production and the Chalmers Centre for Metal Cutting Research (MCR) are acknowledged. The authors would also like to extend their gratitude to Rachid M'Saoubi and Elias Vikenadler from Seco Tools and Martin Selin from Scania CV for the valuable discussions and input.

Appendix

The classic rule of mixture may be used to estimate the stress-strain behaviour of materials. However, this simple rule often does not result in satisfactory predictions for flow stress response of heterogeneous microstructures that include constituents with a significantly different strength, e.g. resistance to deformation or hardness. This is the case for pearlitic-ferritic microstructures in low-alloyed carbon steels with varied amounts of soft ferrite and considerably harder pearlite. To this end, Bouaziz and Buessler [22] proposed an assumption (referred to as Iso-Work) to provide more reliable estimations. This approach essentially assumes an equal work increment in each constituent, allowing for different strain evolution in soft and hard phases/microstructures in the heterogenous materials during the deformation. In regard to pearlitic-ferritic microstructure, this assumption translates to:

$$\sigma_P . d\varepsilon_P = \sigma_\alpha . d\varepsilon_\alpha \tag{1}$$

Here, σ_P and $d\varepsilon_P$ are the average stress and average strain increment in pearlite, and σ_α and $d\varepsilon_\alpha$ refer to the average stress and average strain increment in the ferrite under a given global deformation state. Equation (1) can then be combined with the classic rule of mixture to estimate the overall stress (σ) evolution in the heterogeneous microstructure for a given global strain (ε):

$$\varepsilon = (1 - v_\alpha)\varepsilon_P + v_\alpha \varepsilon_\alpha \tag{2}$$

$$\sigma(\varepsilon) = (1 - v_\alpha)\sigma_P(\varepsilon_P) + v_\alpha \sigma_\alpha(\varepsilon_\alpha) + \sigma_{A-O} \tag{3}$$

where σ_{A-O} accounts for strengthening effect of precipitates and v_α represents the volume fraction of ferrite in the microstructure of steel. The plastic behaviour of ferrite phase can be expressed using the following relationship [51]:

$$\sigma_\alpha = \sigma_0 + \vartheta MG\sqrt{\frac{b(1-exp(-\kappa M\varepsilon_\alpha))}{\kappa d_\alpha}} \tag{4}$$

where $\vartheta = 0.4$ is a constant, M is the Taylor factor and equals to 2.75 for bcc structure, G is the shear modulus of ferrite, and $\kappa = 1$ is the recovery coefficient [51], b is the magnitude of Burgers vector ($= 2.48 \times 10^{-10}$ m), and d_α represents the ferrite average grain size. σ_0 in this equation accounts for the combined effects of lattice friction as well as solid solution strengthening of interstitial and substitutional elements in ferrite [51]:

$$\sigma_0 = 77 + 32\mathrm{Mn} + 678\mathrm{P} + 83\mathrm{Si} + 39\mathrm{Cu} - 31\mathrm{Cr} + 11\mathrm{Mo} + 5544(\mathrm{N}+\mathrm{C}) \tag{5}$$

In this expression, the concentrations of alloying elements are given in weight percent. Moreover, N and C represent the concentrations of carbon and nitrogen dissolved in ferrite. It is worth noting here that Eq. (4) fails to capture the Hall-Petch effect on the yield point; however, it provides satisfactory estimations at larger strains (above 5 %) [51]. The plastic behaviour of pearlite can be described using the following expression [52]:

$$\sigma_P = \sigma_0 + \frac{MGb}{\lambda} + \frac{\eta}{g}\left(1 - exp\left(\frac{-g\varepsilon_P}{2}\right)\right) \tag{6}$$

where λ is the interlamellar spacing of pearlite, while $\eta = 38$ GPa and $g = 70$ are fitting parameters taken from Ref. [52]. σ_0 in this equation is similar to that of ferrite, i.e. Eq. (5).

The strengthening effect of precipitates is estimated by the Ashby-Orowan equation [24]:

$$\sigma_{A-O} = \frac{0.8MGb}{2\pi L\sqrt{1-\upsilon}} ln\left(\frac{x}{2b}\right) \tag{7}$$

where $\upsilon = 0.293$ is the Poisson's ratio and x represents the average diameter of the cross section of carbonitrides on the slip planes, given as:

$$x = \sqrt{\frac{8}{3}}r \tag{8}$$

with r as the mean radius of the precipitates. Under the assumption that the precipitates are distributed randomly in ferrite and pearlite [3], the average spacing between them can be expressed as:

$$L = \sqrt{\frac{2}{3}}\left(\sqrt{\frac{\pi}{v_p}} - 2\right)r \tag{9}$$

where v_p is the volume fraction of precipitates in steel. Equation (7) is shown to provide a more satisfactory estimation of precipitation strengthening in micro-alloyed steels as compared to that of Orowan equation ($\sigma_{Orowan} = 0.8Gb/L$) [24,48]. Combining Equations (4) and (6) with Equation (1) allows to estimate the strain evolution in ferrite for a prescribed strain increment in pearlite using an iterative approach. It is then possible to attain the flow stress of the heterogenous ferritic-pearlitic microstructure in the medium carbon micro-alloyed steels using Eqs. (2) and (3).

Appendix A. Supplementary data

Supplementary data to this article can be found online at https://doi.org/10.1016/j.wear.2024.205632.

Data availability

No data was used for the research described in the article.

References

[1] A. Malakizadi, T. Hajali, F. Schulz, S. Cedergren, J. Ålgårdh, R. M'Saoubi, E. Hryha, P. Krajnik, The role of microstructural characteristics of additively manufactured alloy 718 on tool wear in machining, Int. J. Mach. Tool Manufact. 171 (2021) 103814.

[2] P. Hoier, A. Malakizadi, S. Friebe, U. Klement, P. Krajnik, Microstructural variations in 316L austenitic stainless steel and their influence on tool wear in machining, Wear 428 (2019) 315–327.

[3] T. Baker, Processes, microstructure and properties of vanadium microalloyed steels, Mater. Sci. Technol. 25 (9) (2009) 1083–1107.

[4] M. Binder, F. Klocke, B. Doebbeler, Abrasive wear behavior under metal cutting conditions, Wear (2017) 165–171, https://doi.org/10.1016/j.wear.2017.01.065, 376–377.

[5] S. Ramalingam, P.K. Wright, Abrasive wear in machining: experiments with materials of controlled microstructure, J. Eng. Mater. Technol. 103 (2) (1981) 151–156, https://doi.org/10.1115/1.3224987.

[6] J. Angseryd, E. Olsson, H.-O. Andrén, Effect of workpiece sulphur content on the degradation of a PCBN tool material, Int. J. Refract. Metals Hard Mater. 29 (6) (2011) 674–680, https://doi.org/10.1016/j.ijrmhm.2011.04.016.

[7] N. Ånmark, T. Björk, Effects of the composition of Ca-rich inclusions on tool wear mechanisms during the hard-turning of steels for transmission components, Wear (2016) 173–182, https://doi.org/10.1016/j.wear.2016.09.016, 368–369.

[8] N. Ånmark, T. Björk, A. Ganea, P. Ölund, S. Hogmark, A. Karasev, P.G. Jönsson, The effect of inclusion composition on tool wear in hard Part Turning using PCBN cutting tools, Wear 334–335 (2015) 13–22, https://doi.org/10.1016/j.wear.2015.04.008.

[9] Y. Yamane, H. Usuki, B. Yan, N. Narutaki, The Formation of a protective oxide layer in machining resulphurized free-cutting steels and cast irons, Wear 139 (2) (1990) 195–208, https://doi.org/10.1016/0043-1648(90)90045-C.

[10] S. Ramalingam, B. Von Turkovich, Structure—Property Relations in Free Machining Steels, 1980.

[11] N.E. Luiz, Á.R. Machado, Development trends and review of free-machining steels, Proc. IME B J. Eng. Manufact. 222 (2) (2008) 347–360.

[12] R. Kiessling, Non-Metallic Inclusions in Steel. V, The Institute of Metals, 1989, p. 194, 1989.

[13] S. Ramalingam, J.D. Watson, Inclusion chemistry control for machinability enhancement in steels, Mater. Sci. Eng. 43 (2) (1980) 101–108, https://doi.org/10.1016/0025-5416(80)90136-6.

[14] F.W. Boulger, Machinability of Steels, 1990.

[15] K. Björkeborn, U. Klement, H.-B. Oskarson, Study of microstructural influences on machinability of case hardening steel, Int. J. Adv. Des. Manuf. Technol. 49 (2010) 441–446.

[16] M. Abouridouane, G. Laschet, V. Kripak, J. Dierdorf, U. Prahl, G. Wirtz, T. Bergs, Microstructure-based approach to predict the machinability of the ferritic-pearlitic steel C60 by cutting operations, Procedia CIRP 82 (2019) 107–112.

[17] T. Baker, Microalloyed steels, Ironmak. Steelmak. 43 (4) (2016) 264–307.

[18] A. DeArdo, M. Hua, K.G. Cho, C. Garcia, On strength of microalloyed steels: an interpretive review, Mater. Sci. Technol. 25 (9) (2009) 1074–1082.
[19] H. Exner, Qualitative and Quantitative Surface Microscopy, Physical metallurgy, 1996, pp. 943–1032.
[20] G. Vander Voort, A. Roosz, Measurement of the interlamellar spacing of pearlite, Metallography 17 (1) (1984) 1–17.
[21] J. Liao, G. Qing, B. Zhao, Phase equilibrium studies of the CaO-MgO-Al2O3-SiO2 system for iron blast furnace slag: a review, Metals 13 (4) (2023) 801.
[22] O. Bouaziz, P. Buessler, Iso-work increment assumption for heterogeneous material behaviour modelling, Adv. Eng. Mater. 6 (1-2) (2004) 79–83.
[23] L. Wang, D. Tang, Y. Song, Prediction of mechanical behavior of ferrite-pearlite steel, J. Iron Steel Res. Int. 24 (3) (2017) 321–327.
[24] N. Kamikawa, Y. Abe, G. Miyamoto, Y. Funakawa, T. Furuhara, Tensile behavior of Ti, Mo-added low carbon steels with interphase precipitation, ISIJ Int. 54 (1) (2014) 212–221.
[25] P. Woodard, S. Chandrasekar, H. Yang, Analysis of temperature and microstructure in the quenching of steel cylinders, Metall. Mater. Trans. B 30 (1999) 815–822.
[26] G. Wang, Y. Li, Effects of alloying elements and temperature on thermal conductivity of ferrite, J. Appl. Phys. 126 (12) (2019).
[27] P. Różański, J. Paduch, Modification of non-metallic inclusions in steels with enhanced machinability, Arch. Metall. 48 (3) (2003) 285–307.
[28] S. Pytel, S. Rudnik, The Role of Inclusion Morphology on Machinability of Structural Bar Steels, 1992.
[29] Z. Hong, X. Wu, C. Kun, The influence of aluminium deoxidation and sulphur content on oxide modification and machinability of steel, Steel Res. 66 (2) (1995) 72–76.
[30] N. Åmark, A. Karasev, P.G. Jönsson, The effect of different non-metallic inclusions on the machinability of steels, Materials 8 (2) (2015) 751–783.
[31] H. Liu, W. Chen, Effect of total oxygen content on the machinability of low carbon resulfurized free cutting steel, Steel Res. Int. 83 (12) (2012) 1172–1179.
[32] G. Bittès, F. Leroy, G. Auclair, The relationship between inclusionary deposits and the wear of cutting tools, J. Mater. Process. Technol. 54 (1–4) (1995) 88–96.
[33] C. Leung, L.H. Van Vlack, Solubility limits in binary (Ca, Mn) chalcogenides, J. Am. Ceram. Soc. 62 (11-12) (1979) 613–616.
[34] A. Helle, On the Interaction between Inclusions in Steel and the Cutting Tool during Machining, 1995.
[35] H. Opitz, W. König, ON the wear of cutting tools, in: S.A. TOBIAS, F. KOENIGSBERGER (Eds.), Advances in Machine Tool Design and Research 1967, Pergamon, 1968, pp. 173–190, https://doi.org/10.1016/B978-0-08-003491-1.50013-7.
[36] S. Shoja, S. Norgren, H.-O. Andrén, O. Bäcke, M. Halvarsson, On the influence of varying the crystallographic texture of alumina CVD coatings on cutting performance in steel turning, Int. J. Mach. Tool Manufact. 176 (2022) 103885, https://doi.org/10.1016/j.ijmachtools.2022.103885.
[37] A. Bjerke, F. Lenrick, S. Norgren, H. Larsson, A. Markström, R. M'Saoubi, I. Petrusha, V. Bushlya, Understanding wear and interaction between CVD α-Al2O3 coated tools, steel, and non-metallic inclusions in machining, Surf. Coating. Technol. 450 (2022) 128997.
[38] S. Ruppi, B. Ho, M. Huhtiranta, Wear characteristics of TiC, Ti (C, N), TiN and Al2O3 coatings in the turning of conventional and Ca-treated steels, Int. J. Refract. Metals Hard Mater. 16 (4–6) (1998) 353–368.
[39] S. Subramanian, H. Gekonde, G. Zhu, X. Zhang, U. Urlau, H. Roelofs, Inclusion engineering of steel to prevent chemical tool wear, Ironmak. Steelmak. 31 (3) (2004) 249–257.
[40] Y.D. Yashin, S. Soldatkin, P.Y. Chesnokov, High-machineability steels, Metallurgist 49 (5) (2005) 236–241.
[41] P. Hoier, A. Malakizadi, U. Klement, P. Krajnik, Characterization of abrasion-and dissolution-induced tool wear in machining, Wear 426 (2019) 1548–1562.
[42] A. Slagter, J.A. Setyadji, E.L. Vogt, D. Hernández-Escobar, L. Deillon, A. Mortensen, Nanoindentation hardness and modulus of Al2O3–SiO2–CaO and MnO–SiO2–FeO inclusions in iron, Metall. Mater. Trans. (2024) 1–15.
[43] X. Fang, D. Zhang, An investigation of adhering layer formation during tool wear progression in turning of free-cutting stainless steel, Wear 197 (1–2) (1996) 169–178.
[44] A. Bjerke, A. Hrechuk, F. Lenrick, R. M'Saoubi, H. Larsson, A. Markström, T. Björk, S. Norgren, J.-E. Ståhl, V. Bushlya, Onset of the degradation of CVD α-Al2O3 coating during turning of Ca-treated steels, Wear 477 (2021) 203785.
[45] C. Hu, L. Chen, Z. Zhao, A. Gong, W. Shi, Effects of controlled cooling-induced ferrite–pearlite microstructure on the cold forgeability of XC45 steel, J. Mater. Eng. Perform. 27 (2018) 2772–2781.
[46] A. Marder, B. Bramfitt, Effect of continuous cooling on the morphology and kinetics of pearlite, Metall. Trans. A 6 (1975) 2009–2014.
[47] H. Colpaert, Metallography of Steels: Interpretation of Structure and the Effects of Processing, Asm International, 2018.
[48] T. Gladman, Precipitation hardening in metals, Mater. Sci. Technol. 15 (1) (1999) 30–36.
[49] F. Fang, Q. Yong, C. Yang, S. Hang, A model for precipitation kinetics in vanadium microalloyed steel, J. Iron Steel Res. Int. 17 (2) (2010) 36–42.
[50] B. Dutta, E.J. Palmiere, C.M. Sellars, Modelling the kinetics of strain induced precipitation in Nb microalloyed steels, Acta Mater. 49 (5) (2001) 785–794.
[51] I. Gutiérrez, M. Altuna, Work-hardening of ferrite and microstructure-based modelling of its mechanical behaviour under tension, Acta Mater. 56 (17) (2008) 4682–4690.
[52] S. Allain, O. Bouaziz, Microstructure based modeling for the mechanical behavior of ferrite–pearlite steels suitable to capture isotropic and kinematic hardening, Mater. Sci. Eng., A 496 (1–2) (2008) 329–336.